Imaging of G protein-coupled receptors in solid-supported planar lipid membranes

Marcel Leutenegger[a] and Theo Lasser
Laboratoire d'Optique Biomédicale, École Polytechnique Fédérale de Lausanne, 1015 Lausanne, Switzerland

Eva-Kathrin Sinner
Material Science, Max-Planck-Institut für Polymerforschung, 55128 Mainz, Germany

Rudolf Robelek
Institute of Analytical Chemistry, Chemo- and Biosensors, University of Regensburg, Universitätsstrasse 31, D-93053 Regensburg, Germany

(Received 11 July 2008; accepted 27 November 2008; published 27 January 2009)

This contribution summarizes first some of our efforts in imaging G-protein-coupled receptor (GPCR) functional inserted into planar tethered lipid bilayer membranes (tBLMs) as a novel platform for biophysical studies. The authors introduced recently a novel approach for the functional incorporation of membrane proteins, i.e., by their cell-free expression and *in vitro* reconstitution in the presence of tBLMs. By the combination of the corresponding coding DNA with the protein synthesis machinery of a cell-extract (*in vitro* transcription and translation), the authors observe spontaneous and vectorial insertions of an interesting example of the GPCR family into a tethered bimolecular lipid membrane: the olfactory receptor OR5. After synthesis, imaging of the surface area is performed and the resulting signals are analyzed in order to resolve quantity and lateral mobilities. Ligand-independent aggregation behavior of the GPCRs and quantitative analysis of the fluorescent signals are presented in this work. © *2008 American Vacuum Society.* [DOI: 10.1116/1.3054189]

I. INTRODUCTION

Membrane proteins are important in medicine and life science and play a fundamental role in cell signaling and transmembrane transport. However, membrane proteins such as G protein-coupled receptors (GPCRs) require a lipid bilayer membrane for a correct folding, i.e., a vectorial incorporation for full receptor functioning is mandatory. The common approach of synthesis in a living cell followed by isolation and reincorporation into a model system is complicated, if not impossible, because the functional structure of the protein is likely to be disordered, incomplete or even destroyed. GPCRs are particularly difficult to isolate as a functioning protein, as improper folding already affects their ability of recognizing ligands. Our recent advances in synthetic biology avoid the isolation issue by an *in vitro* expression process of membrane proteins in the presence of model membranes.[1,2] Thereby, the proteins are incorporated into the model membranes *in statu nascendi* and assumed to be correctly folded during synthesis from a cellular extract.

We observed the vectorial and functional incorporations of OR5 in a solid-supported tethered lipid membrane (tBLM). OR5 is an odorant receptor from *Rattus norvegicus* belonging to the vast GPCR family. The incorporation and orientation of the protein were shown by immunolabeling in combination with surface plasmon enhanced fluorescence spectroscopy (SPFS) and reversible ligand binding was shown by surface-enhanced infrared reflection absorption spectroscopy (SEIRAS).[2] Receptor activation, i.e., upon ligand binding, is of primary interest in cell signaling and signal transduction. In general, the activation event itself and the conformation change in the receptor cannot be measured because this would very likely inhibit the receptor function. However based on induced events in the signaling cascade, a few methods for measuring the activation of GPCRs were developed. For instance, Heyse *et al.*[3] and Bieri *et al.*[4] observed the dissociation of the G protein from solid-supported membranes upon photoactivation of incorporated Rhodopsin, which led to a mass change measurable with surface plasmon resonance. In addition, several investigations showed that receptor-ligand binding considerably slows down the diffusion of these receptors, which is, in general, attributed to an aggregation of GPCRs (homo- or heteropolymerization) in the cell membrane to launch the signaling cascade. For instance, Lill *et al.*[5] investigated the signaling kinetics of the neurokinin 1 receptor (NK1R). Initially, this receptor was found to diffuse either fast or slow. The fast fraction diffused with $D \approx 0.21\ \mu m^2/s$ in domains of $\varnothing 1.1\ \mu m$, whereas the slow fraction diffused with $D \approx 0.011\ \mu m^2/s$ within domains of $\varnothing 180$ nm. Within about 1 s after signaling, the diffusion slowed down significantly.

We already showed the vectorial and functional incorporations of OR5 into solid-supported membranes.[2] Here, we quantify the incorporation density and the translational mobility of OR5 using total internal reflection fluorescence (TIRF) imaging and confocal fluorescence correlation spectroscopy (FCS) measurements. Whereas SPFS and SEIRAS measure the average signal from an area of a few

[a]Electronic mail: marcel.leutenegger@a3.epfl.ch

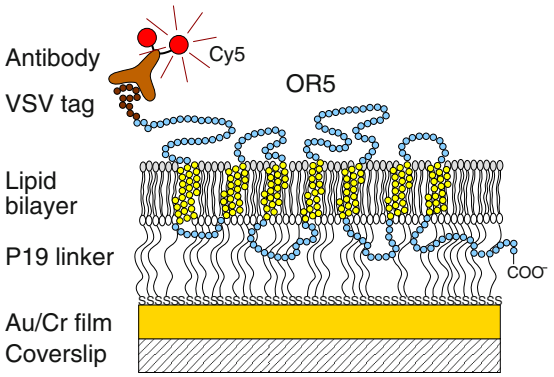

FIG. 1. (Color online) Solid-supported planar lipid membrane assembly with incorporated GCPR. The lipid bilayer consists of a first DMPE monolayer and a second lipid layer from spread PC vesicles. The VSV affinity tag was immunolabeled with a fluorescently labeled antibody.

millimeter,[2] TIRF imaging allows localization and detection of single OR5 receptors in the membrane. Thereby, the amount of incorporated proteins and their spatial organization as well as their mobility were characterized. The incorporation density in the membrane was analyzed with TIRF microscopy and image analysis, which shows that the OR5 density and aggregation increased steadily with expression time. The receptor mobility was investigated with FCS and fluorescence recovery after photobleaching (FRAP) showing that the OR5 was well immobilized within the resolution limits of our instrumentation.

Future investigations will target the detection of receptor-ligand binding events, for instance, by monitoring the lateral mobility of OR5 receptors in our artificial membranes (cf. the review on FCS studies in model membranes by Kahya and Schwille[6]).

II. EXPERIMENTS

Figure 1 outlines the solid-supported tBLM assembly with an incorporated OR5 receptor. The tBLM was prepared on a thin chromium–gold layer of about 5 nm thickness (see Sec. III A). The receptor was expressed with a vesicular stomatitis virus (VSV) affinity tag at either terminus. This VSV tag served as target for immunolabeling with a fluorescently labeled antibody. This antibody was labeled with two Cy5 fluorophores (inferred from FCS of a 5 nM antibody solution and two-step photobleaching of labeled OR5 observed with TIRF microscopy). In contrast to the SPFS measurements, no secondary antibody was required due to the higher detection sensitivity. To probe the orientation of inserted OR5 proteins, cDNA constructs with alternative positions for the tag sequence were used: one cDNA coded for a C-terminal VSV affinity tag, the other for an N-terminal VSV affinity tag.

All experiments were performed in a flow-through microfluidic cell containing a reaction chamber of about 50 μl volume. This chamber was sealed with the metal-coated coverslip providing a window for TIRF measurements. Two inlets at the extremities of the reaction chamber allowed to push/pull liquids through the chamber.

In first control experiments, the background of the metal-coated coverslips and PBS solution was measured. Without chromium, FCS measurements on 5.0 nm gold films suffered from an uncorrelated background count rate of >3 MHz, whereas the chromium-gold sandwich led to <150 kHz background at identical conditions. Therefore, all subsequent experiments were carried out on combined chromium-gold films. Compared to bare coverslips, the coating lowered the observed brightness of the Cy5 fluorophores by about 50% at identical excitation conditions. The relevant detection loss was estimated to be about 30%. (The excitation loss could be compensated by increasing the laser power. For reducing photobleaching, the laser was dimmed such that the count rate of AV-Cy5 was 5–10 kHz per molecule). The presence of tBLMs lowered the background by as much as 30%, possibly due to the lower amount of surface-enhanced Raman scattering from water in contact with the metal coating. The quality of the tBLMs was verified by incubation with the anti-VSV-Cy5 (AV-Cy5) for 10 min prior to the OR5 expression. TIRF images showed that the AV-Cy5 associated only at very few nanometric sites, in average about one site per 20×20 μm^2 area. This association was attributed to defects in the tBLM assembly, i.e., a missing top layer (imperfect vesicle spreading) or a small defect in the underlying metal coating. As these defects showed up much brighter than any other feature, they were readily identified and excluded from further analysis. Finally, it was confirmed that the incorporation of the OR5 did not affect the background fluorescence.

In a next investigation, the vectorial incorporation of OR5 was confirmed. Figure 2 shows representative background corrected and normalized membrane images. Image (a)–(d) show the increase in the spot density and brightness with increasing expression time. Image (e) shows the negative control at 60 min expression of OR5 with the VSV tag at the C′ terminus. If the OR5 is fully incorporated and well oriented, this terminus is buried between the lipid membrane and the metal-coated coverslip as sketched in Fig. 1. This means, the anti-VSV-Cy5 antibody should not be able to bind the tag. Indeed, only a few markers were monitored versus about 150 spots in the case of the N′ terminal tag. These measurements confirm the main results by Robelek *et al.*[2] as they show (1) the vectorial incorporation and (2) the complete incorporation of OR5, (3) the absence of incompletely fused vesicles, and (4) the excellent quality of the artificial membrane, which is intact and nearly defect-free.

In a first attempt, we tried to measure the receptor mobility with FCS. The dual-color instrument with its possibility to measure in a TIRF or confocal configuration was used in the confocal mode. Thereby, premature bleaching of neighboring OR5-AV-Cy5 complexes was minimized. Figure 3(a) shows the intensity traces of a sequence of 5×20 s measurements on incorporated OR5 (90 min expression time) and a trace amount of AV-Cy5 still present after flushing the reaction chamber. The total intensity was composed of three components: a fast bleaching component (39%), a slowly bleaching component (35%), and a "nonbleaching" component (26%) consisting of background and diffusing AV-Cy5.

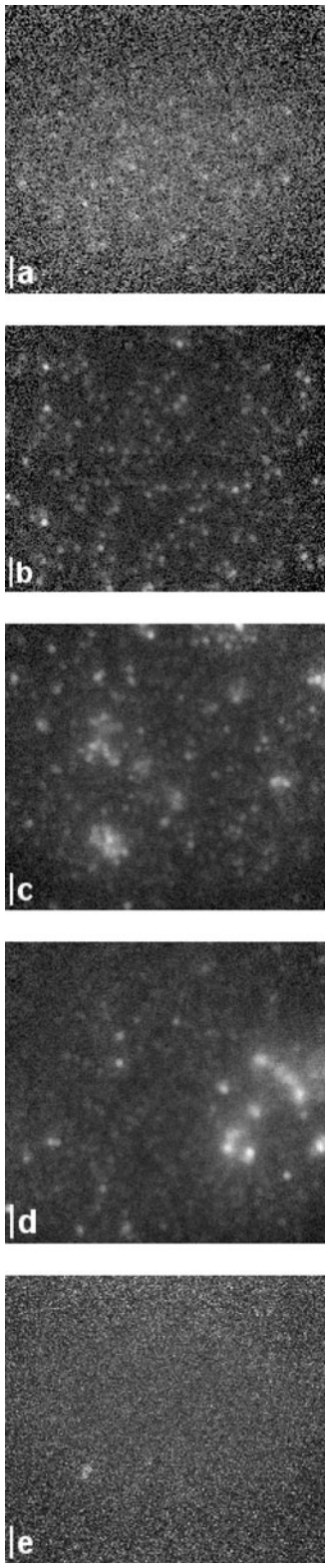

FIG. 2. Background corrected and normalized membrane images vs expression time. (a) 15 min. (b) 30 min. (c) 60 min. (d) 90 min. (e) Negative control after 60 min incorporation of OR5 with a VSV tag at the C′ terminus. Scale bars: 2 μm.

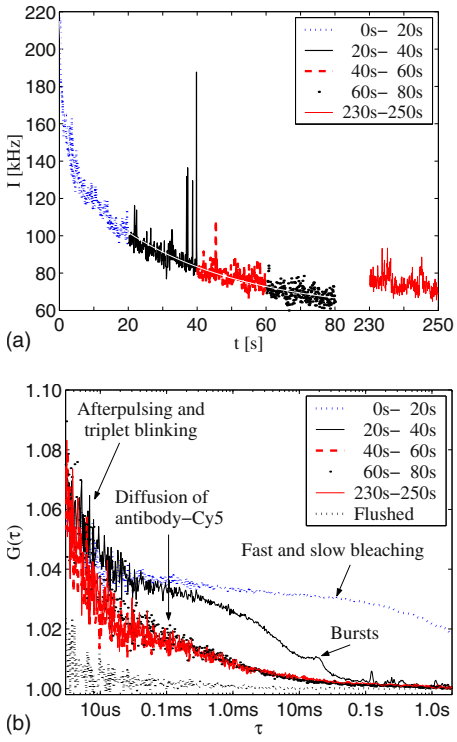

FIG. 3. (Color online) Intensity traces and FCS correlation curves, all taken at the same membrane position. (a) Intensity traces. (b) Autocorrelations.

The fast bleaching fraction had a characteristic bleaching time of about 2.0 s, whereas the slow bleaching occurred at a time scale of about 36 s. The fast component was attributed to photobleaching close to the excitation focus. The slow component was attributed to photobleaching within a larger area of about 1 μm diameter covered by the first side lobes of the excitation field. In this particular measurement, a few intensity bursts at $t \approx 40$ s were presumably due to nonspecifically binding AV-Cy5 or some fluorescent residue of the expression kit. Figure 3(b) shows the corresponding autocorrelation curves. The strong initial bleaching resulted in a stretched decrease in the correlation amplitude. The second correlation curve represents mainly the intensity bursts with a characteristic time of 5–10 ms. The remaining curves are all very similar and represent the diffusion of AV-Cy5 in solution with a diffusion time $\tau_d \approx 0.15$ ms. Before the last measurement, the excitation was interrupted for 150 s. After this interruption, both the fluorescence intensity and the correlation curve reproduced the results of the previous measurement. This behavior was further investigated. A small focus drift by the piezoelectric positioning device was tracked and corrected. This focus drift stretched the diffusion curves shown in Fig. 3(b). Remaining or dissociated AV-Cy5 were flushed with an additional 5 ml of PBS. As a result, except of afterpulsing for lag times $\tau < 5$ μs, no significant correlation amplitude was measured anymore. This result was reproduced on various membrane positions and for several samples. That is we observed freely diffusing AV-Cy5 but could not measure diffusion of OR5. If the OR5 diffuses, it must be so slow that it is below the detection limit set by photobleaching.

Third, slow diffusion was monitored with fluorescence recovery after photobleaching (FRAP). First, the Cy5 was pho-

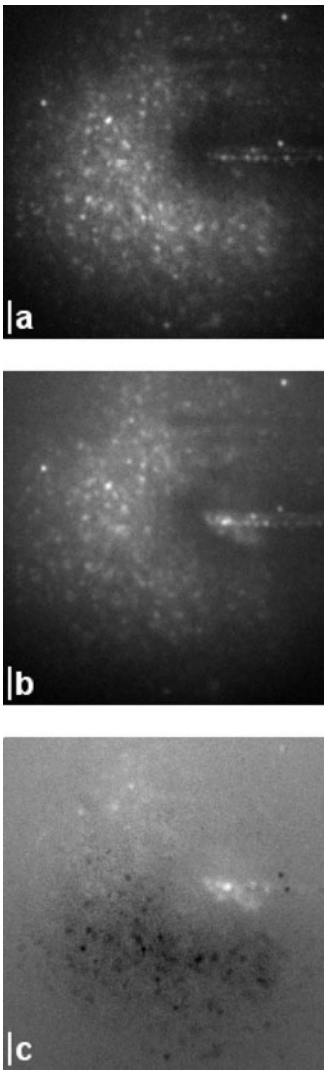

FIG. 4. FRAP experiment. A line and a "U" were bleached and immediately imaged (a). After 6.5 min, a second image was taken (b). The difference picture is shown in (c). Scale bars: 2 μm.

tobleached along a few lines and an image was captured. Later, the same area was imaged several times for checking for recovery after bleaching. Figure 4 shows the result of these FRAP experiments. Image 4(a) and 4(b) were taken with 6.5 min time lapse. The difference image 4(c) shows that the receptors along the single line did not move (up-right corner). The bottom darkened due to a slight focus drift, which moved the excitation area upwards. Inside the "U," a single spot became much brighter, whereas two spots at the right just disappeared. However, the photobleached features did not recover nor an "edge" moving of the bleached pattern could be observed. This finding was confirmed with several FRAP measurements on this sample. For an expression time of 90 min, we never monitored moving receptors although hundreds of charge coupled device (CCD) images were taken from several samples. Taking into account the densely packed, corkscrew-shaped P19 linker immobilizing the tBLM and winding up with the α-helices of the receptor, it would have been surprising if the OR5 diffused above the resolution limit of our instrumentation. Constrained diffusion within small domains was monitored, in particular, at low expression levels favoring OR5 monomers, but the diffusion was typically limited to domains of $<\varnothing 200$ nm (data not shown). These findings are supported by recent studies on GPCRs in living cells and in supported membranes. For instance, Jacquier *et al.*[7] investigated the trafficking of the human odorant receptor OR17–40 in living cells and analyzed their mobility with single particle tracking. The OR17–40 was found to diffuse with diffusion constant in the order of 0.02 $\mu m^2/s$. About 40% were found immobile or constrained within domains of $\approx\varnothing 190$ nm, 49% were diffusing within domains of $\varnothing 300-\varnothing 550$ nm and about 11% were freely diffusing. Moreover, Perez *et al.*[8] showed that GPCRs immobilize upon preparation of supported membranes. These membranes were prepared by detaching the upper part of a cell membrane using a poly-L-lysine substrate. Whereas FRAP experiments performed on living cell membranes showed fast and complete recovery of bleached domains, no recovery was found on supported membranes stating that nearly all GPCRs were immobilized.

We would like to point out that single particle tracking based on TIRF images might be deceptive because the orientation of the observed fluorophore affects the shape of the PSF. When imaging partially immobilized fluorophores as the AV–Cy5, the fluorophore rotation is constrained (just slow and/or limited angular distribution), such that its image appears to wiggle around if the fluorophore changes its orientation. Wiggling was frequently observed at low expression levels, but limited to an area comparable to the PSF size (see Sec. III D). The mobility of the OR5 requires further investigation, as this preliminary analysis does not differentiate between translational and rotational mobility.

Furthermore, the OR5 incorporation density and aggregation were analyzed. Two methods were applied: image segmentation to calculate the spot density SD or Airy density (AD) and ICS to retrieve the cluster density (CD). These methods are briefly introduced in Secs. III B and III C. In a first approach, image segmentation was applied as outlined in Fig. 5. The AD (an improved estimate of the spot density) was then readily obtained with Eq. (13). Figure 6 shows the AD monitored at different expression levels obtained by varying the expression time in steps from 15 to 90 min. The measured AD was then corrected to remove the limitation caused by the size of the PSF according to Eq. (14) with $AD_\infty \approx 2.6\ \mu m^{-2}$. The effective Airy density AD′ showed a linear increase of the OR5 density by $\Delta AD' \approx 0.021\ \mu m^{-2}\,min^{-1}$ starting from $t_0 \approx 8.8$ min. For example, the first OR5 were fully expressed and incorporated within a lead time of about 9 min and the OR5 density increased linearly with the expression time, which is $AD' \approx \Delta AD'(t-t_0)$ for $t > t_0$.

In a second approach, the membrane images were evaluated with ICS as described in Sec. III B. The results are shown in Fig. 7(a), whereas Fig. 7(b) exemplifies a spatial autocorrelation and the corresponding fit on a two-dimensional (2D) Gaussian model curve. The measured CD

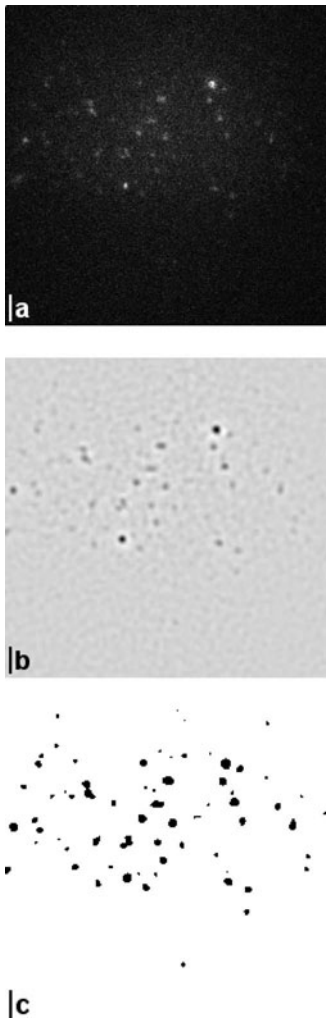

FIG. 5. Image segmentation analysis. (a) OR5-AV-Cy5 complexes. (b) log(3) filtered image. (c) Segmented image. Scale bars: 2 μm.

was about three times larger than the AD. As the cluster density accounts not only for the number of spots but also for the distribution of the spot brightness, CD > AD was expected. Excluding the data points at 15 and 60 min, a linear regression on the data was performed (thin solid line). The lead time was estimated to be 7.6 min, which is in good

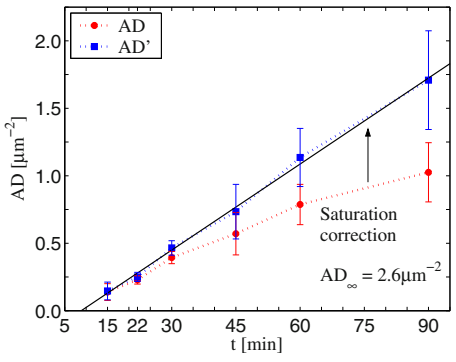

FIG. 6. (Color online) Measured AD and corrected Airy density AD′ vs expression time t. Thin solid curve: linear regression $AD' \approx \Delta AD'(t-t_0)$.

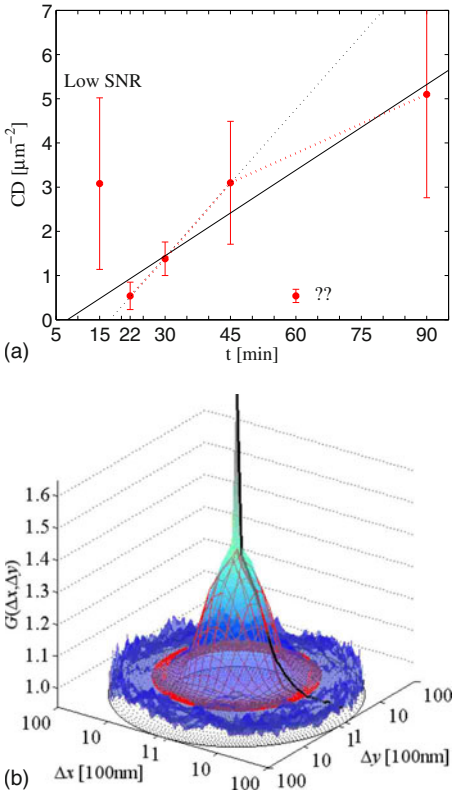

FIG. 7. (Color online) Measured cluster density. (a) Thin solid line: linear regression on data points at 22–45 and 90 min. Thin dotted line: linear regression on data points at 22–45 min with suggested on-set transition and processivity limit. (b) Mesh: fit on 2D Gaussian model curve. (a) Cluster density vs expression time t. (b) Spatial autocorrelation and fit.

agreement with the image segmentation analysis. The CD increased with time by $\Delta CD \approx 0.065\ \mu m^{-2}\ min^{-1}$, that is about $3.1 \times \Delta AD'$. However, the relative scattering of the CD data is significantly larger than for the AD data. The evaluation at 15 min expression time was strongly biased by the low signal to noise ratio [see Fig. 2(a)]. Therefore, the estimation of the CD is about an order of magnitude larger than expected. The evaluation at 22–45 min expression time was much more reliable due to good image contrast and a low number of bright spots. At 60 min, nearly all images showed large-scale aggregates, which led to autocorrelation curves with large waist w. As the contribution to the autocorrelation amplitude is proportional to the square of the feature brightness, these bright large-scale aggregates were the only detectable feature. The resulting CD at 60 min represents therefore the density of large-scale aggregates instead of the protein density. At 90 min, bright aggregates were also monitored but they were organized rather in localized spots instead of extended clouds, which seem to be better mastered with ICS. Nevertheless, the CD at 90 min suffers probably a bias lowering its value. Assuming a linear increase in the OR5 density with expression time, the aforementioned linear regression yields a lower bound of $\Delta CD \geq 0.065\ \mu m^{-2}\ min^{-1}$ and $t_0 \geq 7$ min. In this lower limit, a falling transient for $t > 60$ min (e.g., limited processivity) might account for a slower OR5 expression after about one

hour. Accepting a bias at 90 min, the data points at 20–45 min yield an upper bound of $\Delta CD \leq 0.11\ \mu m^{-2}\ min^{-1}$ and $t_0 \leq 17$ min (thin dotted line). In this upper limit, a rising transient for $t < 20$ min (e.g., setup of dynamic equilibrium) would be required because a lead time of 17 min is clearly disproved by the presence of many spots in images taken after 15 min OR5 expression [Fig. 2(a)]. In this study, ICS was able to monitor the increasing OR5 density but was not reliable enough to allow a precise measurement in the case of low contrast and/or a large distribution of the spot brightness and size. Both limitations are indeed inherited from FCS and known as low signal to noise ratio and molecular brightness distribution.

III. CONCLUSIONS

In summary, the vectorial and complete insertion of OR5 receptors into an artificial tethered membrane assembly were shown. Fluorescence spectroscopy (FCS and FRAP) showed that the incorporated receptors were immobilized. The incorporation density was monitored with ICS and image segmentation. It was shown that the amount of OR5 increased with expression time up to a few receptors or aggregates per μm^2 within 90 min. Moreover, the time for expressing and incorporating a single receptor was estimated to about 9 min. Comparing OR5 distributions at different expression times revealed that the first OR5 were incorporated at random positions. Thereafter, a tendency of incorporating several OR5 side by side was observed, presumably due to ribosomes staying in contact with the membrane in between two expression cycles.

Image segmentation and spot analysis were very robust but did systematically underestimate the OR5 density. Because the measured Airy densities were well below the measurement limit, this bias could be removed using Eq. (14) and the measured PSF area. On the other hand, the ICS analysis provides, in principle, an unbiased estimation of the receptor density but became unreliable in the case of a low image contrast or in presence of OR5 aggregates. Both methods indicate a lead time of roughly 10 min required to fully express and incorporate the first receptors. Image segmentation showed then a linear increase of the OR5 density with expression time of about $0.021\ \mu m^{-2}\ min^{-1}$, whereas this value ranged between 0.065 and $0.11\ \mu m^{-2}\ min^{-1}$ with the correlation analysis.

In addition, preliminary FCS measurements were performed in order to monitor receptor-ligand binding. Due to the immobilized receptors, these measurements suffered from rapid photobleaching of the Cy5 labels and failed. Future experiments may benefit from the dual-color performance of our TIRF fluctuation spectroscopy instrument. For instance, Förster resonant energy transfer in combination with dual-color TIRF imaging should enable monitoring the aggregation of receptors or the receptor-G protein interaction upon ligand binding.

In order to achieve translational diffusion of incorporated GPCRs, investigations are in preparation to render the artificial membrane more fluid. The density and nature of the attachment layer are of particular interest for achieving an optimal compromise between lateral mobility and axial immobility. Using a small amount of fluorescently labeled lipid molecules, the lateral membrane mobility will be monitored with FCS. The axial mobility of the membrane is already subject of investigation with optical coherence tomography (OCT) and spectral interferometry.

A. Sample preparation

1. Preparation of chromium-gold layer

Standard glass coverslips (150 μm thick, Menzel-Gläser, Braunschweig, Germany) were cleaned and sonicated for 20 min in 2% Hellmanex II (Hellma, Müllheim/Baden, Germany), rinsed with bidistilled water, dried and oxygen plasma cleaned. Planar gold surfaces were prepared by evaporating a 1.5 nm thick chromium adhesion layer (99.99%, œrlikon balzers coating, Brügg, Switzerland) and a 3.5 nm thick gold layer (>99.99%, Metalor technologies SA, Neuchâtel, Switzerland) in an Edwards Auto 306 evaporation system at 5×10^{-6} mbar. The evaporation rate was kept below 0.5 nm/min. A thin chromium adhesion layer was required to obtain a hard gold coating (pale gray brown) instead of porous and granulous gold deposits (brilliant blue appearance). Adding the chromium layer also lowered the background luminescence of the gold film by more than an order of magnitude.

2. Preparation of tBLM

The tBLM was then prepared in a flow cell following the protocol by Robelek *et al.*[2] This preparation of the tBLM was recently monitored with surface plasmon resonance spectroscopy by Wiltschi *et al.*[9]

3. In vitro expression of OR5-VSV

A "T7 TNT Quick *in vitro* expression system" (Promega, USA) was used. The reactions were prepared according to the supplier's instruction. The incubation was performed in a thermoblock at 30.3 ± 0.3 °C for 15–90 min.

4. Labeling of the OR5-VSV

The OR5-VSV was immunolabeled *in situ* by incubating with Cy5 labeled anti-VSV primary antibodies. After 10 min, the excess labels were rinsed with PBS solution while monitoring the content of free labels with confocal FCS measurements. The PBS solution was then exchanged against a Gloxy antioxidant/PBS solution, which reduced the photobleaching to about 1/3 as compared to PBS.

B. Image correlation spectroscopy

The random spatial distribution of the incorporated OR5 was analyzed with ICS. This method and its limitations were discussed in detail by Petersen *et al.*[10] ICS analyzes the spatial auto- or cross correlation of the images I and J. The spatial cross correlation C of I and J is defined by

$$C(\Delta x,\Delta y) = I(x,y) * J(x,y) = \iint I(x+\Delta x, y+\Delta y)J(x,y)dxdy, \quad (1)$$

where Δx and Δy are the lag distances. As usual, the spatial autocorrelation is obtained by setting $J=I$. For digital images, the fast Fourier transform can be used for calculating the correlation as a convolution of $I(-x,-y)$ and $J(x,y)$. The normalized spatial cross correlation is given by

$$G(\Delta x,\Delta y) = \frac{I * J}{\langle I\rangle\langle J\rangle} = \frac{\langle I(x+\Delta x,y+\Delta y)J(x,y)\rangle}{\langle I(x+\Delta x,y+\Delta y)\rangle\langle J(x,y)\rangle}, \quad (2)$$

where $\langle\ \rangle$ denotes the spatial average. With this equation, "infinitely" large images of homogeneously excited samples can be treated because the lateral extent is unbounded. For treating images of finite extensions, a symmetric normalization should be applied such that the normalization takes into account the effective overlap between I and J upon cross correlation. For this purpose, a general mask W can be introduced for defining a weighted average with weight $W(x,y) \in [0,1]$ at point (x,y). Equation (2) is then generalized for images of finite size and arbitrary shape (defined by $W\neq 0$), e.g.,

$$G(\Delta\vec{r}) = W * W\frac{(IW) * (JW)}{((IW) * W)(W * (JW))}, \quad (3)$$

with $\Delta\vec{r}=(\Delta x,\Delta y)$. The factor $W*W$ corresponds to the effective overlap as it stands for the cumulated weight at lag distances Δx and Δy, whereas the denominator is the product of the weighted average of the images I and J within the same window W. The performance of this normalization is outlined in Fig. 8. The correlation amplitude G_0 of about 0.2 is reproduced to less than 5% difference independently of the choice of the mask W. At large lag distances, the difference ΔG is dominated by stochastic noise with zero mean and about 0.01 amplitude. The correlation amplitude G_0 is defined by

$$G_0 = \lim_{\Delta\vec{r}\to 0}(G(\Delta\vec{r})) - \lim_{\Delta r\to\infty}(G(\Delta\vec{r})) = \lim_{\Delta\vec{r}\to 0}(G(\Delta\vec{r})) - G_\infty, \quad (4)$$

where the offset $G_\infty \approx 1$ is the correlation amplitude at large lag distances. The amplitude G_0 equals the variance of the normalized intensity fluctuations. If the intensity is an accurate representation of the sample density, its variance is also the variance of the density fluctuations, which equals the inverse of the average occupation number N_p:

$$G_0 = \frac{\langle (I-\langle I\rangle)^2\rangle}{\langle I\rangle^2} = \mathrm{var}(\Delta_n I(\vec{r})) = \mathrm{var}(\Delta_n c(\vec{r})) = \frac{1}{N_p}. \quad (5)$$

The occupation number N_p gives the number of receptors (particles) in the observation volume, which is defined by the PSF of the TIRF microscope. Considering the EMCCD camera (Andor Luca, monochrome) as an array of square sized pixels ($9\times 9\ \mu\mathrm{m}^2$, 80% fill factor) in a 10 μm grid, the PSF for a single active element can be calculated as described by

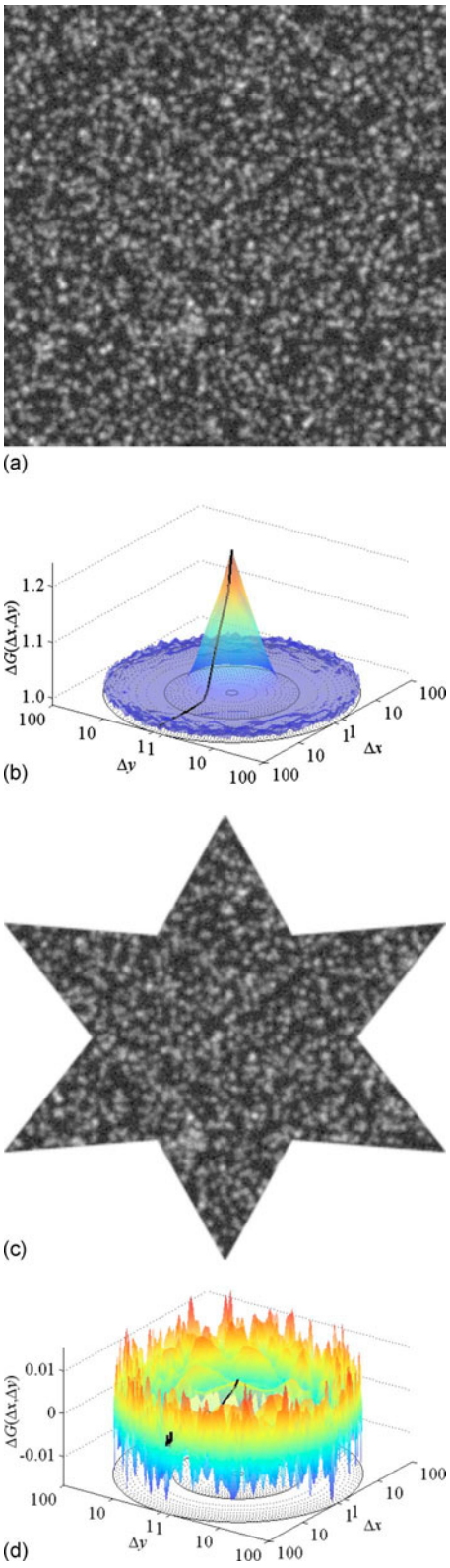

FIG. 8. (Color online) Invariance of the autocorrelation $G(\Delta\vec{r})$ for different masks $W(x,y)$. The images were 256×256 pixels in size. In order to emphasize the correlation amplitude near the coordinate origin, $G(\Delta\vec{r})$ is represented in polar coordinates with logarithmic radius Δr. The correlation is represented for lag distances $\Delta r<100$ pixel. The black curve represents the average amplitude along the radius. (a) Image intensity I with uniform mask $W=1$. (b) Autocorrelation $G_{I\times I}(\Delta\vec{r})$. (c) Image intensity $J=IW$ with star-shaped mask W. (d) Difference $\Delta G=G_{I\times I}-G_{J\times J}$.

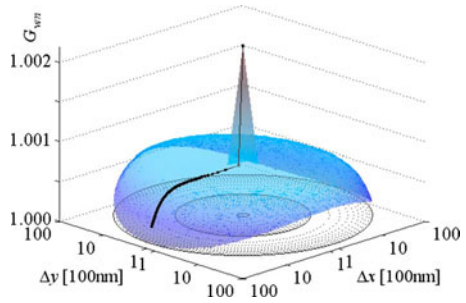

FIG. 9. (Color online) Background correlation $G_{wn}(\Delta\vec{r})$. The projected CCD pixel size is 100 nm.

Leutenegger and Lasser.[11,12] In this study, it is sufficient to calculate a cross section for a fluorophore 10 nm above the glass interface as this is approximately the glass–(OR5–AV–Cy5) distance. According to Petersen *et al.*,[10] the receptor density is therefore given by the cluster density

$$\mathrm{CD} = \frac{1}{G_0 A} = \frac{N_p}{A}, \tag{6}$$

where A is the area of this PSF cross section:

$$A = \frac{1}{\mathrm{PSF}(0)} \int \mathrm{PSF}(\vec{r})\mathrm{d}\vec{r}. \tag{7}$$

If the cross section is approximately Gaussian with waist w, the area can be estimated by fitting $G(\Delta\vec{r})$ on a 2D Gaussian centered near the origin. The model function for fitting the spatial image correlation is therefore given by

$$G(\Delta\vec{r}) = G_\infty + G_0 \exp\left(-\frac{|\Delta\vec{r} - \vec{r}_0|^2}{w^2}\right), \tag{8}$$

where $\vec{r}_0$ accounts for small image drifts in cross-correlation measurements. The waist of the fitted Gaussian is defined by the PSF. Hence, the area A can be estimated by $A \approx \pi w^2$.

1. Fitting

Images of single receptors or small receptor aggregates show intensity spots of the size of the PSF. This size can be measured independently for unspecifically binding molecules. If the fitted waist w differs by more than about 30%, the data should be rejected as the image probably contains features similar or larger in size than the PSF. Alternatively, these features can be masked by defining a matching window W. Due to the limited size of the images, the offset G_∞ shows variations in the order of $\sqrt{N_A}/N_A$, where N_A is the number of PSF areas in the window W. It was shown[13] that the fit should include only data in the correlation function $G(\Delta\vec{r})$ for $\Delta r < 3w$. Using proper normalization this constraint can be relaxed to $\Delta r < s/2$, where s is the smallest dimension in the window W.

2. Corrections

In general, the intensity fluctuations are due to several sources, i.e., the sample of interest (s), nonspecific fluorescence (ns), autofluorescence (a), and background (wn). Except the background, these sources show fluctuations with the characteristic dimension of the PSF. The background has the characteristics of white noise and contributes not to the correlation except at the origin where it can be dominant. Therefore, the amplitude $G(0)$ at the origin was excluded from the fits. Assuming that these sources are independent as they are from different components, the measured correlation is given by

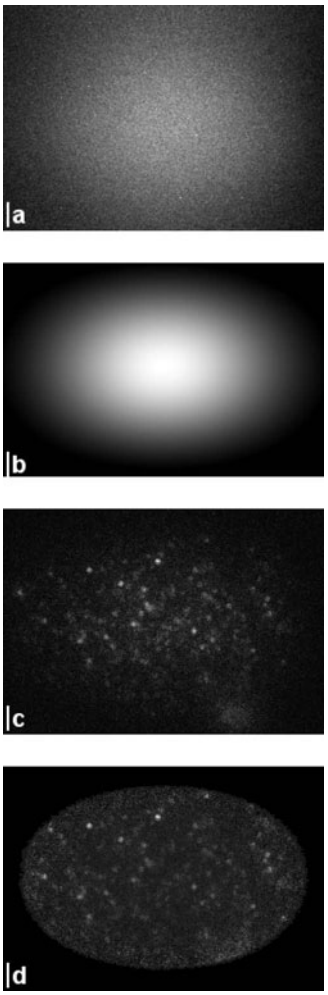

FIG. 10. Applied image correction. (a) The background I_{wn} was first subtracted from (c) the measured image I. The result was then divided by the excitation profile P_{ex} (b). The correlation was performed on the corrected image I_c (d), where the window W covers the region where $P_{ex}(x,y) > 0.2$, that is an elliptical area of 23×15 $\mu\mathrm{m}^2$ extension on the membrane. Scale bars: 2 μm.

$$g(\Delta\vec{r}) = \sum_i g_i(\Delta\vec{r})\langle I_i\rangle^2, \tag{9}$$

where $g(\Delta\vec{r}) = G(\Delta\vec{r}) - 1$ is the correlation of $\delta I_i(x,y) = I_i(x,y) - \langle I_i\rangle$, that is $g_\infty \approx 0$ and $g_0 = G_0$. The fitted correlation amplitude G_0 can be corrected according to

$$G_{s0} = \frac{G_0\langle I\rangle^2 - G_{ns0}\langle I_{ns}\rangle^2 - G_{a0}\langle I_a\rangle^2}{(\langle I\rangle - \langle I_{ns}\rangle - \langle I_a\rangle - \langle I_{wn}\rangle)^2}. \tag{10}$$

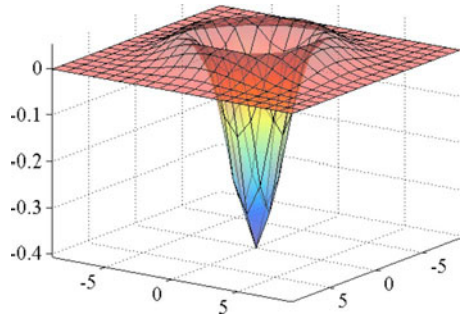

FIG. 11. (Color online) Laplacian-of-Gaussian filter of width 3. All units in pixel (100 nm).

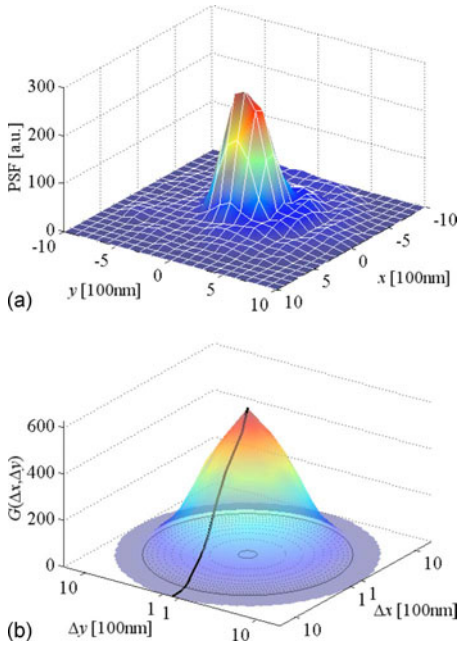

FIG. 12. (Color online) Imaging point spread function and its autocorrelation. (a) Image PSF. (b) Autocorrelated PSF.

3. Analysis

The instrument background, the autoluminescence of the metal-coated coverslip and the autofluorescence of the bare tBLM was measured *a priori*. This combined background $I_{wn}(x,y)$ had white-noise characteristics as the autocorrelation confirmed (see Fig. 9).

The slow variation stems from the envelope of the background intensity as outlined in Fig. 10(a). Instead of correcting the background contribution with Eq. (10), the background was subtracted from the image intensity *a priori*. This was required for normalizing the image intensity with the inhomogeneous excitation intensity $I_{ex}(x,y)$. The excitation intensity was estimated by fitting the average background corrected intensity of a large number of images on a model distribution (modulated 2D Gaussian). The correlation was then performed on the homogenized images I_c given by

$$I_c = \frac{I - I_{wn}}{P_{ex}}, \tag{11}$$

where P_{ex} is the fitted excitation intensity profile but normalized to unit amplitude. Figure 10 outlines the applied correction.

The contribution from nonspecific fluorescence and autofluorescence was estimated by measuring a sample prepared according to the protocol given in Sec. III A, but with no coding DNA added to the *in vitro* expression kit. Thereby, the membrane was exposed to the expression kit as well as the labeled antibody. However, these contributions turned out to be negligible, such that the OR5 cluster density was estimated directly with Eq. (6).

C. Image segmentation

If the cluster density CD is lower than about $1/A$, where A is the PSF cross section (see Sec. III D), individual spots can be resolved. In this case, image segmentation methods can estimate the CD based on a spot analysis.

1. Spot density

For calculating the SD, the images were first filtered with a Laplacian-of-Gaussian filter of width 3 [LOG(3), see Fig. 11] to remove noise and enhance the edges.[14] A threshold was then applied and the resulting segments were analyzed in shape and brightness. The spot density is readily given by

$$\mathrm{SD} = \frac{N_s}{A_{ex}}, \tag{12}$$

where N_s is the number of spots (segments) identified in the excitation area A_{ex} of the image. As Fig. 5(c) shows, the applied segmentation method found the majority of spots but with areas proportional to the spot brightness. The spot density yields a lower bound of the OR5 density as it accounts large aggregates exactly like a single receptor. Therefore, at least a first order correction should be applied to account for the area of large aggregates.

2. Airy density

Given the spot area A_s, the number of spots N_s can be estimated with the cumulated spot area normalized by the PSF cross section A. Therewith, N_s accounts for A_s and would be biased by the spot brightness if no further correction were applied. For instance, dim spots were identified as small spots of a few image pixels only as exemplified in Fig. 5(c). This bias can be corrected in first order by taking the maximum brightness I_s of each spot into account. For a given LOG filter and threshold setting, the relation $A_s(I_s)$ can be estimated by calculating the segment area $A_{PSF}(I_s)$ obtained for the measured PSF image with identical peak brightness I_s. Taking the peak brightness as parameter is justified as it is most likely included in the segmented spot area. Therefore, an improved estimation of the receptor density is given by

$$\mathrm{AD} = \frac{1}{A_{\mathrm{ex}}} \sum \frac{A_s}{A_{\mathrm{PSF}}(I_s)}, \tag{13}$$

which we called area or Airy density as N_s is estimated based on the PSF cross section. The Airy density removes the bias caused by large-scale aggregation, but removing the bias due to microaggregation within an area $<A$ requires further investigation. Due to the PSF cross section A, the AD saturates at a value $\mathrm{AD}_\infty \approx 2/3A$, which is approximately the limit of detecting individual spots. Therefore, the effective Airy density AD′ is given by correcting the measured AD according to

$$\mathrm{AD}' = \frac{\mathrm{AD}_\infty \mathrm{AD}}{\mathrm{AD}_\infty - \mathrm{AD}}. \tag{14}$$

A second order correction would consist in breaking large spots into segments of an area $A_s \approx A$. Thereby, large intensity fluctuations within a spot could be taken into account. This correction was not required as the few very large spots had a quite narrow intensity distribution, such that the correction factors for subsegments would not scatter much.

D. Point spread function

The detection PSF was measured by averaging the image of several bright spots. Figure 12(a) shows the measured PSF, which was in good agreement with an Airy pattern except for an asymmetry in the Airy rings. This asymmetry might be due to a partially polarized fluorescence emission. However, the bright spots used for this measurement were attributed to a large number of Cy5, such that the polarization should be neglectable. The PSF cross section was evaluated with Eq. (7) and $A = 0.26\ \mu\mathrm{m}^2$ was obtained. This corresponds to a waist $w = 0.29\ \mu\mathrm{m}$, which is in excellent agreement with the calculated Airy radius of $0.28\ \mu\mathrm{m}$ for a wavelength of 670 nm. The autocorrelation of the measured PSF served as reference for classifying the ICS fits ($w_{\mathrm{PSF}} = 0.47\ \mu\mathrm{m}$).

ACKNOWLEDGMENTS

The authors thank Samuel Terrettaz and Pedro Pascoal, LCPPM-EPFL, for assistance, in metallizing coverslips; Carolyn Yong, LMBM-EPFL, for sample storage; André Galliker, Lot-Oriel, for support with the EMCCD camera; and Matthias Geissbühler and Joseph Lasser, LOB-EPFL, for digging through the data heap. The authors acknowledge funds from the European Commission (FuSyMEM project, Sixth Framework Programme) and the Swiss National Science Foundation (Grant No. 200021-103333).

[1] R. Robelek, F. D. Stefani, and W. Knoll, Phys. Status Solidi A **203**, 3468 (2006).
[2] R. Robelek, E. S. Lemker, B. Wiltschi, V. Kirste, R. Naumann, D. Oesterhelt, and E.-K. Sinner, Angew. Chem., Int. Ed. **46**, 605 (2007).
[3] S. Heyse, O. P. Ernst, Z. Dienes, K. P. Hofmann, and H. Vogel, Biochemistry **37**, 507 (1998).
[4] C. Bieri, O. P. Ernst, S. Heyse, K. P. Hofmann, and H. Vogel, Nat. Biotechnol. **17**, 1105 (1999).
[5] Y. Lill, K. L. Martinez, M. A. Lill, B. H. Meyer, H. Vogel, and B. Hecht, ChemPhysChem **6**, 1633 (2005).
[6] N. Kahya and P. Schwille, Mol. Membr Biol. **23**, 29 (2006).
[7] V. Jacquier, M. Prummer, J.-M. Segura, H. Pick, and H. Vogel, Proc. Natl. Acad. Sci. U.S.A. **103**, 14325 (2006).
[8] J.-B. Perez, J.-M. Segura, D. Abankwa, J. Piguet, K. L. Martinez, and H. Vogel, J. Mol. Biol. **363**, 918 (2006).
[9] B. Wiltschi, W. Knoll, and E.-K. Sinner, Methods **39**, 134 (2006).
[10] N. O. Petersen, C. Brown, A. Kaminski, J. Rocheleau, M. Srivastava, and P. W. Wiseman, Faraday Discuss. **111**, 289 (1999).
[11] M. Leutenegger and T. Lasser, Opt. Express **16**, 8519 (2008).
[12] M. Leutenegger, "Single molecule detection on surfaces," Ph.D. Thesis, EPFL, 2007, http://library.epfl.ch/theses/?nr=3854.
[13] A. G. Benn and R. J. Kulperger, Environmetrics **7**, 167 (1996).
[14] D. Marr and E. Hildreth, Proc. R. Soc. London, Ser. B **207**, 187 (1980).